10-2010

Exciton antennas and concentrators from core-shell and corrugated carbon nanotube filaments of homogeneous composition

Jae-Hee Han
Massachusetts Institute of Technology

Geraldine LC Paulus
Massachusetts Institute of Technology

Ryuichiro Maruyama
Sony Corp.

Daniel A. Heller
Massachusetts Institute of Technology

Woo-Jae Kim
Kyungwon University

See next page for additional authors

Han, Jae-Hee; Paulus, Geraldine LC; Maruyama, Ryuichiro; Heller, Daniel A.; Kim, Woo-Jae; Barone, Paul W.; Lee, Chang Young; Choi, Jong Hyun; Ham, Moon-Ho; Song, Changsik; Fantini, C; and Strano, Michael S., "Exciton antennas and concentrators from core-shell and corrugated carbon nanotube filaments of homogeneous composition" (2010). *Birck and NCN Publications.* Paper 666. http://dx.doi.org/10.1038/nmat2832

Authors

Jae-Hee Han, Geraldine LC Paulus, Ryuichiro Maruyama, Daniel A. Heller, Woo-Jae Kim, Paul W. Barone, Chang Young Lee, Jong Hyun Choi, Moon-Ho Ham, Changsik Song, C Fantini, and Michael S. Strano

Exciton antennas and concentrators from core–shell and corrugated carbon nanotube filaments of homogeneous composition

Jae-Hee Han[1,2]†, Geraldine L. C. Paulus[1]†, Ryuichiro Maruyama[3], Daniel A. Heller[1], Woo-Jae Kim[4], Paul W. Barone[1], Chang Young Lee[1,2], Jong Hyun Choi[5], Moon-Ho Ham[1], Changsik Song[1], C. Fantini[6] and Michael S. Strano[1,2]★

There has been renewed interest in solar concentrators and optical antennas for improvements in photovoltaic energy harvesting and new optoelectronic devices. In this work, we dielectrophoretically assemble single-walled carbon nanotubes (SWNTs) of homogeneous composition into aligned filaments that can exchange excitation energy, concentrating it to the centre of core–shell structures with radial gradients in the optical bandgap. We find an unusually sharp, reversible decay in photoemission that occurs as such filaments are cycled from ambient temperature to only 357 K, attributed to the strongly temperature-dependent second-order Auger process. Core–shell structures consisting of annular shells of mostly (6,5) SWNTs ($E_g = 1.21\,\mathrm{eV}$) and cores with bandgaps smaller than those of the shell ($E_g = 1.17\,\mathrm{eV}$ (7,5)–$0.98\,\mathrm{eV}$ (8,7)) demonstrate the concentration concept: broadband absorption in the ultraviolet–near-infrared wavelength regime provides quasi-singular photoemission at the (8,7) SWNTs. This approach demonstrates the potential of specifically designed collections of nanotubes to manipulate and concentrate excitons in unique ways.

There is renewed interest in developing photonic materials for optical concentration[1,2] and photon collection[3,4] for applications such as higher-efficiency photovoltaic cells[5] and infrared photoemitters/photodetectors[6]. One-dimensional materials, such as inorganic nanowires[3] and carbon nanotubes[7–13], are promising candidates for this because of their aligned axial transition dipoles[7–9], large absorption cross-sections and high quantum efficiencies[10–12]. In the case of SWNTs, photonic applications have been hampered by an inability to separate and sort them as optically distinct species[9,14–16]. Recent advances in our laboratory[15] and elsewhere[16] have enabled this separation on preparative scales. Although the photophysics of isolated, single carbon nanotubes and heterogeneous aggregates has been extensively studied[7–13], these new separation methods allow us to construct optically homogeneous materials of dimensions much larger than typical excitation wavelengths of interest, enabling new photonic structures.

Optical properties of SWNT bundles have been studied abundantly using Rayleigh and Raman scattering[7–9], photoluminescence excitation (PLE) and absorption spectroscopy[10–13]. As a result, diameter- and distance-dependent exciton energy transfer (EET; also referred to as Förster resonance energy transfer[17]) from larger-bandgap semiconducting SWNTs to smaller-bandgap ones within bundles in solution has been illustrated[10–13]. Recently, EET was elegantly examined[13] within a single pair of SWNTs, highlighting the potential for such species to form more complex antenna structures and concentrators. The systems explored in our work create such structures. Time-resolved spectroscopy of

SWNT bundles reveals extremely rapid excited-state relaxation (1 ps) compared with isolated SWNTs (ref. 18). This behaviour has been attributed to energy transfer from the semiconducting to the metallic SWNTs within each bundle[19], followed by rapid non-radiative carrier cooling in the metallic nanotubes[20]. SWNT bundles have also found applications in the solar energy field; they can, for example, be used to replace the transparent electrode in organic solar cells[5]. However, none of these applications so far has considered optically homogeneous SWNT bundles, which have only recently become available in preparative quantities[15,16] for photonic applications.

The improvement of photonic devices by increases in quantum efficiency as well as power conversion efficiency has been an important research focus for many decades. For example, EET between shorter- and longer-wavelength dyes was used to develop tandem organic solar concentrators with high efficiency[1]. Microconcentrator photovoltaics using soft-lithographically moulded replicas of commercially available lens arrays was demonstrated to increase total output power[2]. In the field of nano-optics, engineering nanostructure plays a critical role in the control of propagating light in photonic applications such as optical antenna structures[3,4,6].

In this work, (6,5) semiconducting SWNTs were isolated and dielectrophoretically spun into largely homogeneous solid filaments. A small residual amount of (7,6) SWNTs leads to a surprisingly large amount of EET in the (6,5)-enriched fibre. We also find that the photoluminescence quantum yield of these fibres unexpectedly decays sharply as they are heated to only

[1]Department of Chemical Engineering, Massachusetts Institute of Technology, Cambridge, Massachusetts 02139, USA, [2]Institute for Soldier Nanotechnologies, Massachusetts Institute of Technology, Cambridge, Massachusetts 02139, USA, [3]Advanced Material Laboratories, Sony Corporation, Kanagawa, 243-0021, Japan, [4]Department of Energy and Biological Engineering, Kyungwon University, Seongnam, Gyeonggi-do 461-701, South Korea, [5]School of Mechanical Engineering, Birck Nanotechnology Center, Bindley Bioscience Center, Purdue University, West Lafayette, Indiana 47907, USA, [6]Departamento de Física, Universidade Federal de Minas Gerais, Belo Horizonte, MG 30123-970, Brazil. †These authors contributed equally to this work. *e-mail: strano@mit.edu.
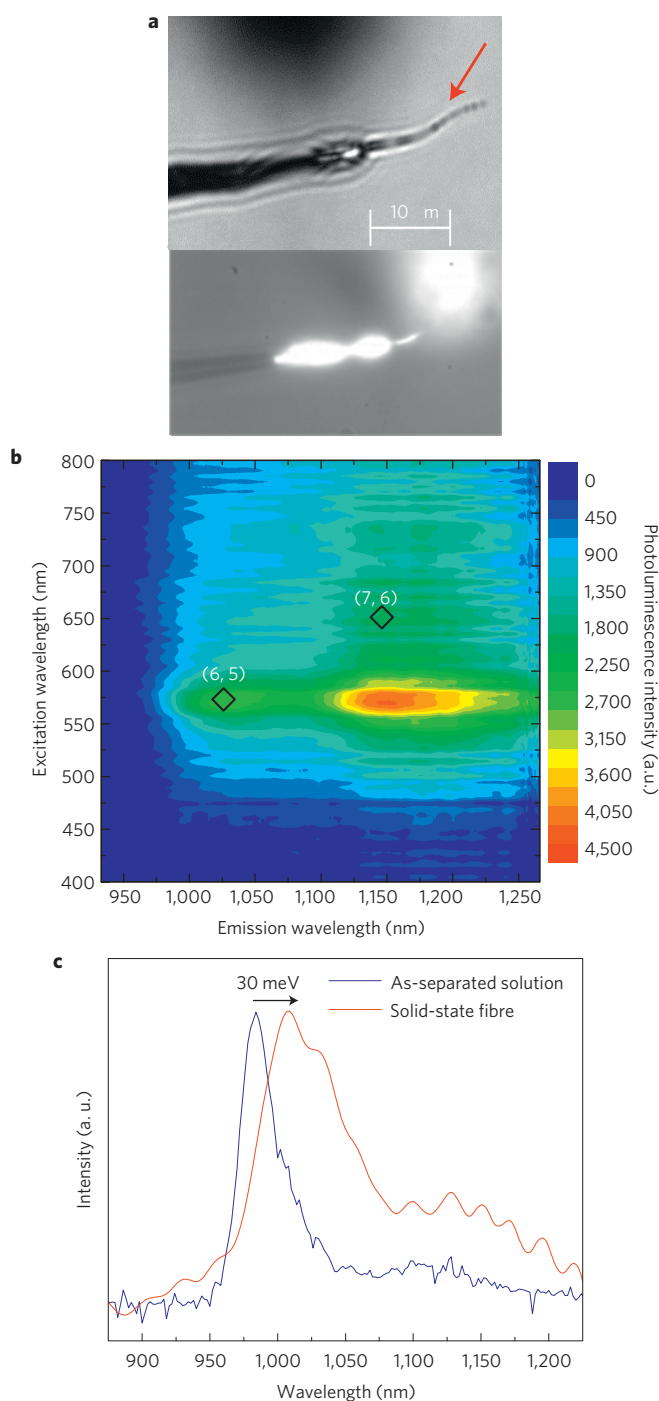
Figure 1 | Optical properties of a (6,5)-enriched SWNT fibre: photoluminescence and strong EET. a, Upper panel: an optical image of a SWNT fibre supported on a tungsten tip; lower panel: a corresponding two-dimensional near-infrared InGaAs photoluminescence image (with 658-nm-wavelength laser excitation, 1 mW), showing bright photoluminescence from the very end of the fibre in a solid state, confirming a high degree of semiconductor purity. Note that the light emission at the upper-right corner is due to a halogen lamp source. **b,** A corresponding PLE map demonstrating the majority of (6,5) chirality. **c,** The photoluminescence spectra of both an As-separated solution and a solid-state fibre taken at 570-nm-wavelength monochromatic light excitation, corresponding to the E_{22} transition of individual (6,5) SWNTs in an aqueous solution[10]. Note that the peak of the fibre (solid red line, ~1,008 nm) is redshifted (by about 30 meV) from that of individual SWNTs in an aqueous solution (solid blue line, ~984 nm).

357 K with recovery on cooling them back to room temperature. This behaviour is attributed to Auger recombination. We then construct core–shell structures where the SWNT composition determines the absorption bandwidth and where EET is controlled through gradients in the optical bandgap of the different SWNTs making up the shell and the core. These structures form antennas that funnel excitons to their core and emit in the near-infrared regime, creating unique photonic devices and optical concentrators.

Electronically homogeneous fibres of diameters up to 4 μm were created using a mechanically automated dielectrophoresis (DEP) drawing apparatus (see Supplementary S1, Fig. S1). The DEP technique[21] assembles an aligned fibre of controlled length and diameter from a SWNT solution in 2% sodium cholate surfactant. Solutions of homogeneous SWNT species were prepared by single cascades of the density-gradient ultracentrifugation method[15,16] (Supplementary S2, Fig. S2). Figure 1a is an optical micrograph of a typical fibre, with bright photoluminescence shown under 658 nm with 1 mW illumination, imaged with a near-infrared InGaAs array with 1 s exposure. Both an absorption (Supplementary Fig. S3) and a PLE profile (Fig. 1b) carried out directly on the fibre confirm that it contains mostly (6,5) SWNTs (~99 mol%) with minority compositions of (7,6) SWNTs (~1%) and remaining species comprising <1%. Fibre formation is known to perturb the electronic and exciton transport properties for SWNTs through inter-tube coupling[14,22]. The (6,5) SWNTs have an emission maximum that is 30 meV redshifted from its value of 1.26 eV in the starting solution, shown in Fig. 1c. The result for this fibre, containing 3.3×10^7 SWNTs, is consistent with that of another study, which used Rayleigh scattering spectroscopy to measure E_{11} redshifts in the range of tens of millielectronvolts on bundling. This energy shift in the fibre states is understood to be a result of mutual dielectric screening of the excitons by neighbouring SWNTs. In summary, our fibres are analogous to several recently investigated bundled systems, including SWNT dimers[13] and surface-grown bundles[12], with the key exception that they contain 10^7 times as many SWNTs in structures that are larger than the wavelength of the absorbing light.

We first study the inherent EET observed between the abundantly present (6,5) SWNTs and the minority (~1 mol%) (7,6) nanotubes still present after enrichment of the former in the fibre. Figure 2a,b shows typical near-infrared PLE maps of a fibre (Fig. 2a, inset) taken at temperatures of 298 K and 357 K, respectively. Peaks are assigned to the photoluminescence of the (6,5) and (7,6) SWNTs. The fibre was suspended under a blanket of ultrahigh-purity nitrogen (>99.999%) (3 l min⁻¹) at controlled temperatures (298–357 K) using a thermal-isolation microscope stage (Linkam). Although the fibre is irradiated with light of 570 nm (the E_{22} excitation wavelength for (6,5) SWNTs) and contains only ~1% (7,6) nanotubes, the resulting photoluminescence from the (7,6) nanotubes is most significant. In fact, a calculation of the quantum yield (defined as the ratio of photons emitted to photons absorbed) shows that it is about two orders of magnitude larger for the (7,6) SWNTs than for the (6,5) SWNTs (Fig. 2c). This effect is due to the EET between the two types of SWNT. Another interesting phenomenon is the evolution of the spectral intensity with temperature: the photoluminescence intensity data (Fig. 2d) show a decrease in photoluminescence of both the (6,5) and (7,6) SWNTs with increasing temperature. The decrease becomes more significant at higher temperatures. The quantum yield of the whole fibre itself, shown in Fig. 2e, indicates a similar decay. This transition is reversible, repeatable and not related to environmental or morphological changes (Supplementary S4). A theoretical model is developed to provide a plausible explanation for this trend. Taking into account the different pathways for

exciton generation and decay, the following system of ordinary differential equations is set up:

$$\frac{dN_{1(6,5)}}{dt} = G_{(6,5)} - k_{EET}N_{1(6,5)} - k_r N_{1(6,5)} - k_d N_{1(6,5)}$$
$$- k_a N_{1(6,5)}(N_{1(6,5)} - 1) + k_{2-1}N_{2(6,5)} \quad (1)$$

$$\frac{dN_{2(6,5)}}{dt} = \frac{1}{2}k_a N_{1(6,5)}(N_{1(6,5)} - 1) - k_{2-1}N_{2(6,5)} \quad (2)$$

$$\frac{dN_{1(7,6)}}{dt} = G_{(7,6)} + k_{EET}N_{1(6,5)} - k_r N_{1(7,6)} - k_d N_{1(7,6)}$$
$$- k_a N_{1(7,6)}(N_{1(7,6)} - 1) + k_{2-1}N_{2(7,6)} \quad (3)$$

$$\frac{dN_{2(7,6)}}{dt} = \frac{1}{2}k_a N_{1(7,6)}(N_{1(7,6)} - 1) - k_{2-1}N_{2(7,6)} \quad (4)$$

In this scheme, N denotes the total amount of excitons in the system, with subscript 1 (2) referring to excitons for which the energy difference between the electron and the hole equals E_{11} (E_{22}), and subscripts $(6,5)$ and $(7,6)$ denote the chirality of the nanotubes. Here, G is the exciton generation rate calculated on the basis of the extinction coefficient of the fibre (estimated using Beer's law to be $5.07 \times 10^5 \, m^{-1}$, (taking into account scattering)), the incident power density of the light ($4.1 \, \mu W$), the spot size of the incident light ($1.69 \times 10^{-13} \, m^2$) and the illuminated area of the fibre ($1.11 \times 10^{-12} \, m^2$). For the $(6,5)$ SWNTs, this leads to an estimated exciton generation rate $G_{(6,5)}$ of 6.47×10^{12} excitons s^{-1}. The amount of excitons generated on the $(7,6)$ tubes is considerably smaller (6.53×10^{10} excitons s^{-1}). As discussed earlier, in bundles, excitons on 'donor' $(6,5)$ nanotubes can transfer to 'acceptor' $(7,6)$ nanotubes through EET (refs 10–13), and this is represented by a first-order reaction with rate constant k_{EET}. It is expected that k_{EET} is several orders greater than k_r (ref. 10). Excitons can decay through radiative relaxation, resulting in the formation of photons detected as photoluminescence. The temperature-dependent reaction rate constant k_r for this first-order reaction is governed by a simple interpolation formula[23]:

$$\frac{1}{k_r} = \tau_r = \tau_{min} \times \frac{T}{T_{min}} \exp\left(\frac{T_{min} - T}{T}\right)$$

where τ_{min}, T_{min} and T are the minimum radiative lifetime, its corresponding temperature and the environmental temperature, respectively. Both τ_{min} and T_{min} show a diameter dependence:

$$\tau_{min} \approx \tau_0 + \alpha d$$

$$T_{min} \approx \frac{\beta}{d}$$

where both α and β are the proportionality factors in the correlation, and d is the tube diameter. The best-fit values for the three parameters are: $\tau_0 = 12 \, ns$, $\alpha = 24 \, ns \, nm^{-1}$ and $\beta = 272 \, K \, nm$ (ref. 23). As shown in Fig. 2f the temperature dependence of k_r is rather weak in the temperature range considered in this experiment. For both types of SWNT, k_r is of the order of $10^7 \, s^{-1}$. The excited electron–hole pairs can also recombine non-radiatively (thus giving rise to lattice vibrations), mediated by defects along the nanotube's length or by the nanotube's ends[24]. The defect-mediated decay rate constant k_d is well described with classical Arrhenius kinetics[25,26]: $k_d = k_{d,0}\exp(-E_{A,d}/k_B T)$, where $k_{d,0}$ is the pre-exponential factor, $E_{A,d}$ is the activation energy, k_B is the Boltzmann constant and T is the temperature of the fibre. A final possible excitonic decay channel in the SWNT fibre is exciton–exciton annihilation (otherwise known as the 'Auger' process). In this case, the bimolecular reaction $2N_1 \xrightarrow{k_a} N_2 + GS$ describes how, on the collision of two excitons at

the E_{11} level, one is annihilated (decays to the ground state, GS), and the energy that is being released in the collision is used to promote the other exciton to the E_{22} level. Given the nature of this exciton–exciton annihilation mechanism, we propose to describe the temperature dependence using collision theory[27], which results in a modified Arrhenius expression where the prefactor shows a $\sqrt{T}$ dependence: $k_a = k_{a,0}\sqrt{T}\exp(-E_{A,a}/k_B T)$, where $k_{a,0}$ is the pre-exponential factor and $E_{A,a}$ is the activation energy. The N_2 exciton quasi-immediately relaxes back to the E_{11} level with a rate constant $k_{2-1} = 2.3 \times 10^{13} \, s^{-1}$ (ref. 28). As the excitons on the E_{22} level are very short-lived intermediates, one can employ the pseudo-steady-state approximation to equations (2) and (4), leading to an expression for $N_{2(6,5)}$ and $N_{2(7,6)}$, which can then be plugged into equations (1) and (3) respectively. The final system of ordinary differential equations to be solved numerically is then reduced to

$$\frac{dN_{1(6,5)}}{dt} = G_{(6,5)} - k_{EET}N_{1(6,5)} - k_r N_{1(6,5)} - k_d N_{1(6,5)}$$
$$- \frac{1}{2}k_a N_{1(6,5)}(N_{1(6,5)} - 1)$$

$$\frac{dN_{1(7,6)}}{dt} = G_{(7,6)} + k_{EET}N_{1(6,5)} - k_r N_{1(7,6)} - k_d N_{1(7,6)}$$
$$- \frac{1}{2}k_a N_{1(7,6)}(N_{1(7,6)} - 1)$$

With knowledge of G and k_r, a fit of the model to the data (Fig. 2d) results in values for k_{EET}, k_d and k_a for every data point (Fig. 2f). The value of k_{EET} is found to be reasonably invariant with temperature at $6.24 \pm 1.19 \times 10^9 \, s^{-1}$, as expected[17]. An analysis of the EET efficiency (η_{EET}) is included in Supplementary S4a. The defect-related rate constant equals $k_d = 10^{10}\exp(-0.17 \, eV/k_B T)$, where the value for the activation barrier is in agreement with values found elsewhere in the literature[26]. The second-order Auger rate constant becomes $k_a = 10^{10}\sqrt{T}\exp((-0.1937 \, eV \pm 0.028494 \, eV)/k_B T)$. A comparative analysis of the value of k_a found here to values in the literature is included in Supplementary S4b. It is worth mentioning that the activation energy for this Auger process shows a small variation with temperature (see inset of Fig. 2f). This is not uncommon for multistep reactions in solids[29–31]. The Auger process is a combination of a diffusion step and a reaction step (one exciton gets promoted to the E_{22} level, the other one is demoted to the ground state). Therefore, the effective Auger rate constant k_a used in the model can be written as

$$\frac{1}{k_a} = \frac{1}{k_D} + \frac{1}{k_R} \quad (5)$$

where k_D and k_R are the rate constants for the diffusive and the reaction step, respectively. From equation (5), one can easily deduce the effective activation energy of the Auger process to be

$$E_{A,a} = \frac{E_{A,D}k_R + E_{A,R}k_D}{k_D + k_R}$$

As both k_D and k_R vary with temperature, $E_{A,a}$ is also temperature dependent. Taking into account that k_a is a second-order rate constant, it is clear that exciton–exciton annihilation (or the Auger process) is the most efficient decay channel in the fibre. The non-radiative decay channel is much more efficient than its radiative counterpart, and is responsible for the low photoluminescence quantum yields of the fibres in this work, 10^{-3}–10^{-4} (Fig. 2e), values that are similar to those reported in the literature for much smaller bundle systems[22,32]. A similar analysis has been carried out on an average data set, containing data taken while heating the sample, while subsequently cooling it, and during a repeat of this hysteresis experiment six days later (Supplementary S4c).

As suggested by the near-infrared micrograph in Fig. 3a, we find considerable spatial heterogeneity in the emission density along the length of such fibres. This spatial variation also
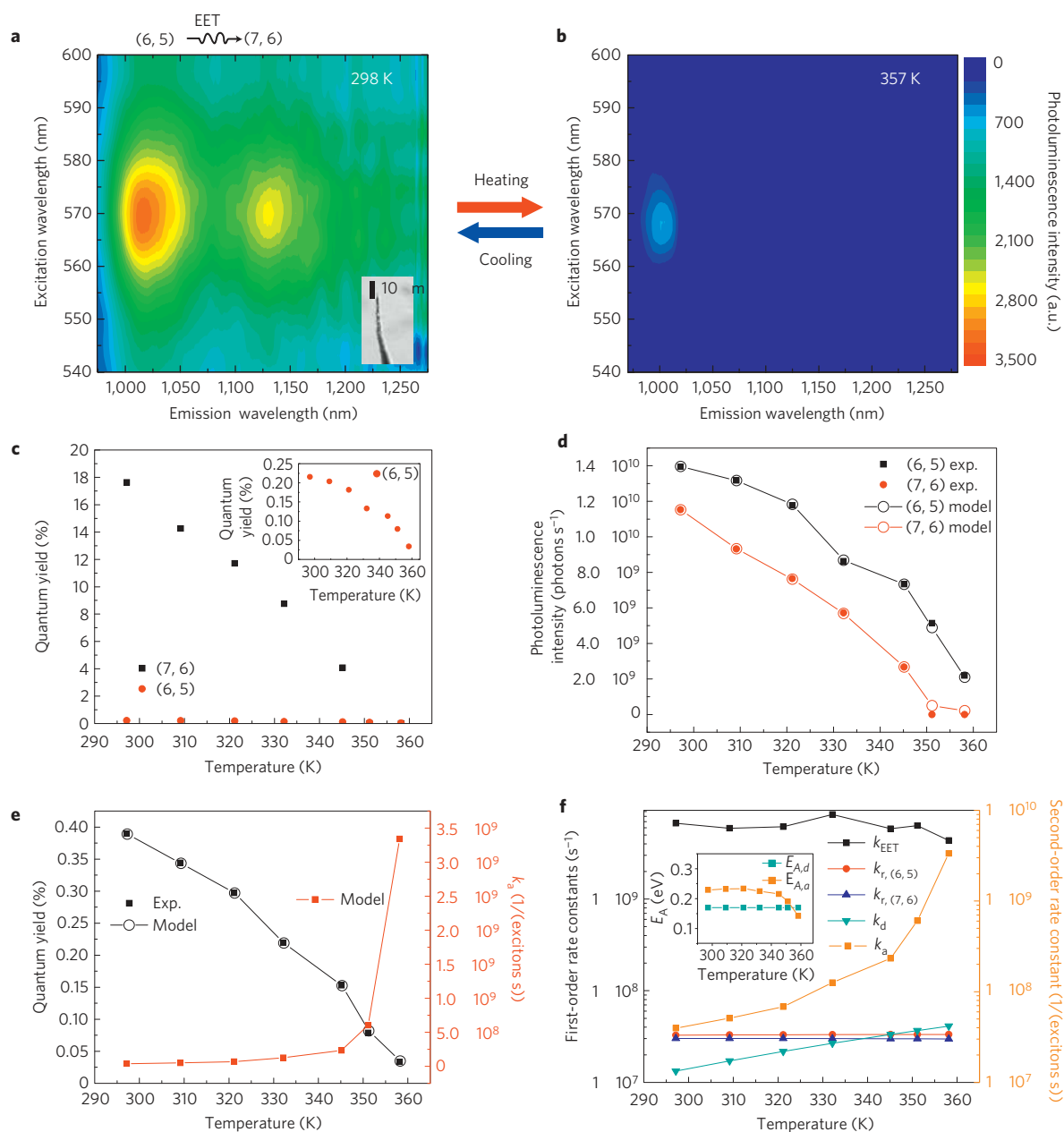
Figure 2 | PLE map and reversible photoluminescence change as a function of temperature. a,b, Typical near-infrared (970–1,280 nm) PLE maps of a fibre (inset of **a**) taken at temperatures of 298 (**a**) and 357 K (**b**). **c**, Quantum yield of both types of SWNT present in the fibre versus temperature (the quantum yield is defined as the ratio of photons emitted to photons absorbed). Inset: The quantum yield of the (6, 5) tube on a different scale. **d**, Photoluminescence intensities of both (6, 5) and (7, 6) emissions versus temperature (both experimental data and model fit). **e**, Quantum yield of the fibre (both experimental data and its fit) versus the temperature, demonstrating a monotonic decrease with increasing temperature. The Auger rate constant k_a is largely responsible for the strong decrease in the quantum yield with temperature. **f**, Temperature dependence of all of the first- and second-order rate constants in the system, calculated from theory ($k_{r,(6,5)}, k_{r,(7,6)}$) or from numerical simulations based on the model developed (k_{EET}, k_d, k_a). Inset: The dependence of the activation barrier of both k_d and k_a on temperature.

undergoes a remarkable transition with temperature, and again in an approximately reversible manner. Figure 3a shows a higher-resolution near-infrared intensity map of the total relative density around a fibre of 1.6 µm diameter suspended on a N$_2$-blanketed thermal-isolation microscopy stage. Localized regions of high emission intensity are clearly visible along the length of the fibre. On progressive heating from 298 to 357 K, these regions broaden and become delocalized. Cycling the system back to 298 K repeatedly confirms that this delocalization is reversible and not associated with thermal annealing or impurity desorption. Although the images resemble the spatial heterogeneity observed in near-field

investigations of single carbon nanotubes, invariably created by lattice defects, it is important to note that the images in Fig. 3a arise from an ensemble collection of approximately 2.4×10^8 SWNTs, so sidewall defects cannot explain the phenomena. Furthermore, the localization lengths (2–5 µm) are longer than the range of nanotube lengths (100–1,000 nm); therefore, nanotube ends, which are known to be strong centres of irradiative recombination[11,24], cannot be responsible.

The phenomenon was further investigated by adapting the near-infrared photoluminescence microscope to split the collection image in photon energy using a pass filter with wavelength
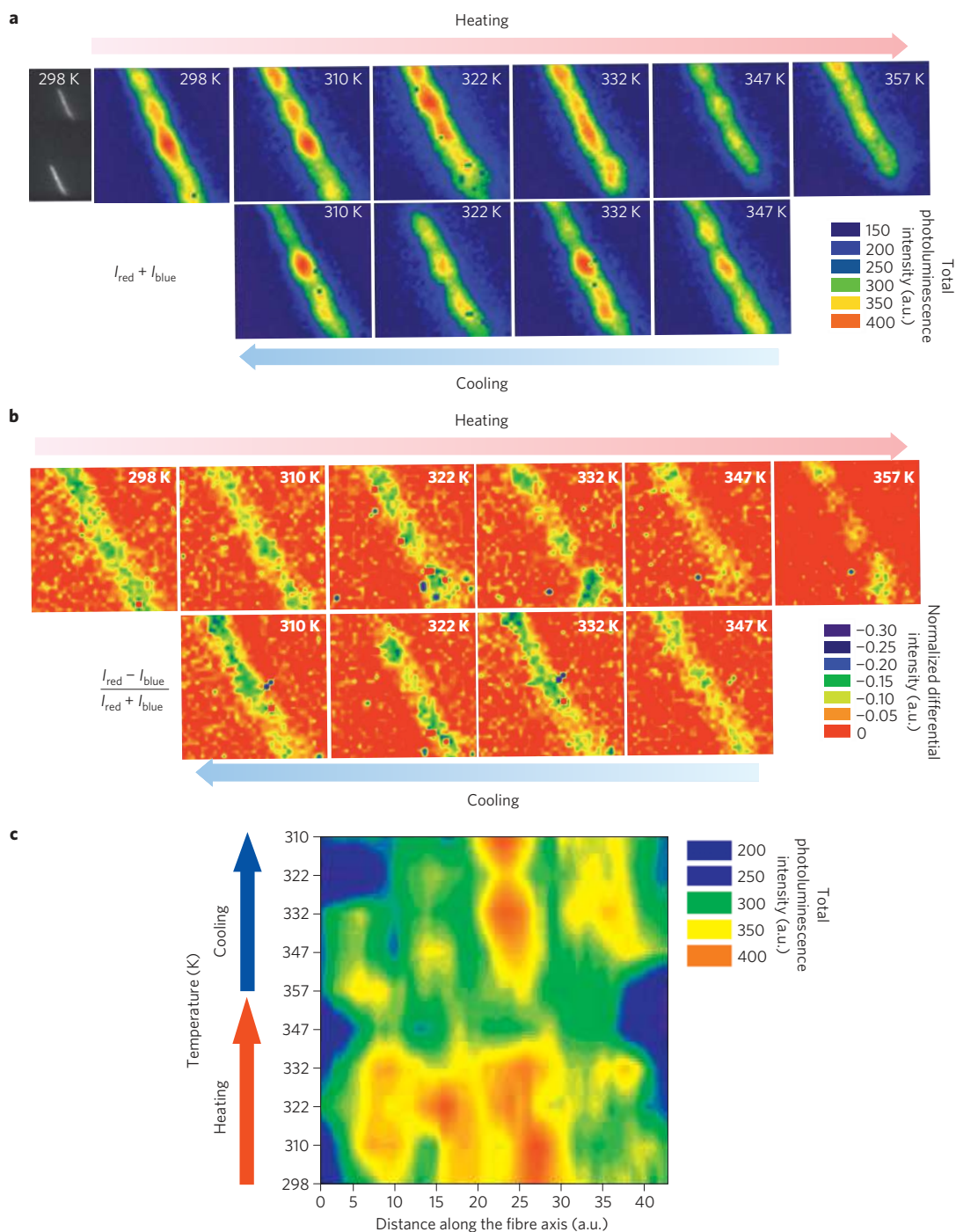
Figure 3 | Spatially resolved, temperature-dependent photoluminescence behaviour under an in-house-built dual-channel microscope.
a, Temperature-evolutional, high-resolution near-infrared photoluminescence intensity maps of the total relative density around a fibre suspended on a thermal-isolation microscope stage blanketed with continuous, ultrahigh-purity N_2 (>99.999%) with a flow rate of $3\,l\,min^{-1}$. **b**, Normalized differential intensity contour plots of the same fibre, mapping spatial variations with temperature in the local emission energy (see main text and Supplementary S6 for details). **c**, A detailed close-up of the photoluminescence intensity along the fibre axis showing a reversible recovery of the energy with temperature.

centred at 1,090 nm. This yielded a pair of images, named 'red' and 'blue', corresponding to long- and short-pass wavelengths, respectively (see Supplementary S5 for details on the microscope and a typical photoluminescence spectrum of the fibre). To map the spatial variations in the local emission energy (Fig. 3b), the normalized intensity difference between both images is calculated: $(I_{red} - I_{blue})/(I_{red} + I_{blue})$. The resulting mapping reveals that the localized regions of high intensity seen in Fig. 3a are blueshifted relative to the mean value for the whole fibre (Fig. 3b). With

increasing temperature, there is a net emission energy loss that recovers with cycling back to 298 K (Fig. 3c). As the relative variation in redshift is observed to be of the same order between bundled and isolated SWNTs (30 meV), we hypothesize that the relatively blueshifted regions are associated with increased inter-tube spacing or decreased physical density along the fibre length. This is supported by the fact that the regions are spatially of the order of the persistence length of a SWNT bundle[33]. The fact that these blueshifted regions have higher intensities (as
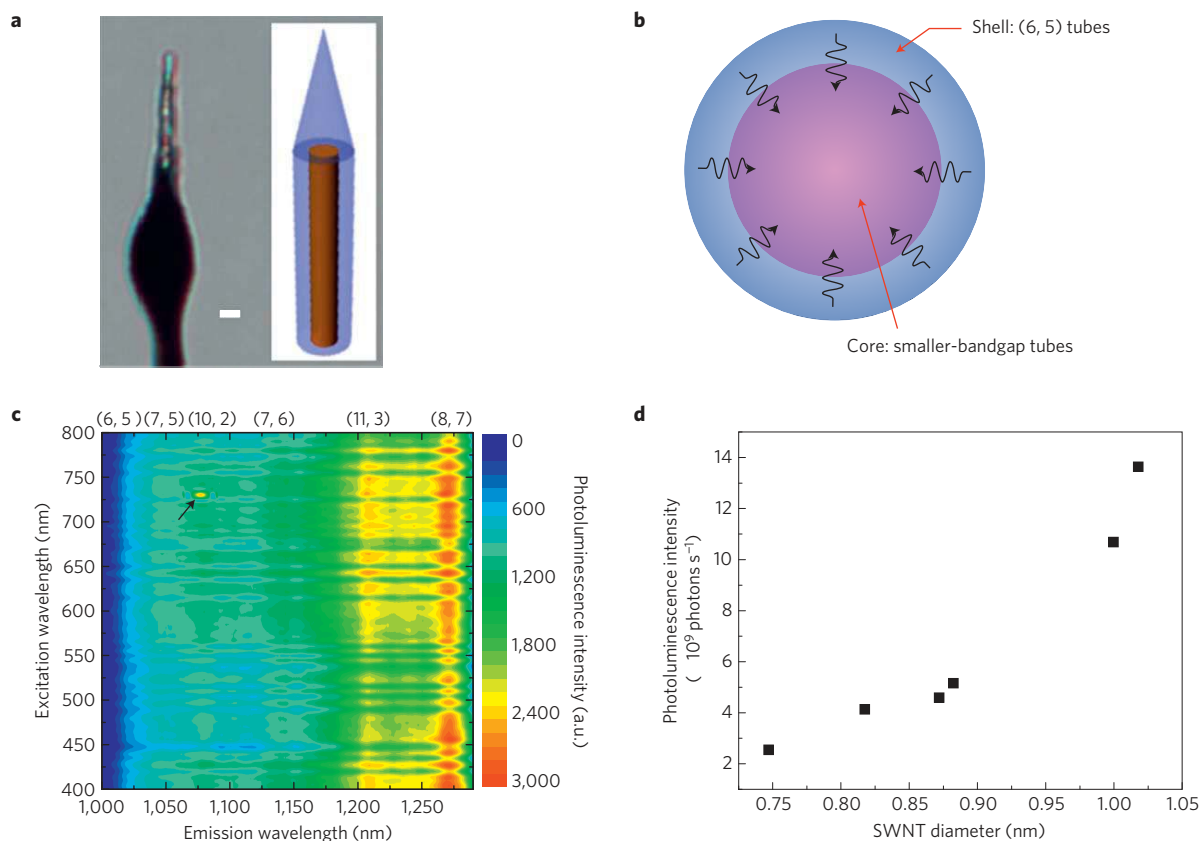
Figure 4 | Development of an exciton antenna from a core–shell carbon nanotube structure. a, An optical image of the exciton antenna (scale bar, 2 μm) with a schematic. **b**, A top view of the antenna structure, where the curved black arrows indicate the inward EET on photoexcitation. **c**, The resulting excitation profile, demonstrating the dominant emission produced from the smallest-bandgap element (8, 7) on photoexcitation over a broad range extending from ultraviolet to near-infrared wavelengths. **d**, Experimental data showing the photoluminescence intensity for each type of SWNT in the exciton antenna for excitation at 570 nm and at room temperature.

indicated by Fig. 3a) could be because they contain more nanotubes, although packed in a less dense manner. The larger volume of these regions is also visible in a scanning electron microscope image (Supplementary Fig. S6a). More details on the correlation between the density and the degree of the wavelength shift in the different regions of the fibre are discussed in Supplementary S6.

A carbon nanotube fibre can potentially form unique types of optical antenna structure, distinct from porphoryin systems[34] and photosynthetic proteins[35], in that the excitons are one-dimensionally quantum confined, but can successively transfer energy to a central concentrator element through EET. We explored this possibility by forming a fibre consisting of successive shells with larger-bandgap SWNTs radiating outward. The effect is to transfer excitons through an efficient EET pathway to a central core, thereby realizing a concentration effect. To this end, our SWNT separation procedure, published elsewhere[15], was used to create a solution of primarily small-bandgap SWNTs, forming the collector core. A (6, 5)-enriched SWNT solution was then successively deposited creating an absorbing shell (Fig. 4a,b). The multistep DEP fibre formation creates the desired core–shell structure, but the tip contains solely (6, 5) SWNTs (Fig. 4a). The distribution of chiralities and their concentrations for the core is found to be: [(8, 7), 28.4%], [(11, 3), 10.5%], [(7, 6), (26.3%)], [(10, 2), 5.26%], [(6, 5), 8.42%], [(7, 5), 8.42%], [(9, 1), 6.32%] and [(6, 4), 6.32%]; a derivative method[16] has been used to estimate these values. Figure 4c is the resulting excitation–emission PLE profile, and it is clear that the dominant emission is produced by the smallest-bandgap (8, 7) SWNTs, when the fibre itself is excited over a broad range extending from the ultraviolet to near-infrared

wavelengths. Figure 4d shows the resulting photoluminescence from the nanotubes as a function of their diameters (and thus their bandgaps). As the excitons are funnelled to the central core of the fibre, a spatial concentration is realized. The transfer is shown to be extensive, with most species showing no radiative recombination within our detection limits. However, curiously some residual emission is detected from the larger bandgap (10, 2) (marked by an arrow in Fig. 4c). As this component is present only as a minority, and it is unlikely that it is preferentially enriched at the core–shell interface, this may be evidence for an anomalously low EET efficiency for the (10, 2) species. The EET efficiencies depend linearly on the energy difference between the donor and the acceptor[13] (and thus their chiralities). However, EET also depends on the fractions of every type of nanotube in the fibre as well as their spatial distribution in the core–shell structure.

We note that there is the potential to enhance existing single-nanowire or single-carbon-nanotube photovoltaic devices, particularly if one creates an axial conductive core along which excitons can be split and harvested, as in the case where the core is one terminal of a p–n junction[36]. The concept of successive annular shells that behave as exciton concentrators has yet to be extended to inorganic nanowire devices[34].

The optical antenna approach in this work is similar to biological methods of photon concentration that have been studied extensively[35,37,38]. Photosynthetic reaction centres in plant photosynthesis, for example, contain light-harvesting antennas that funnel excitation to a specific location, such as the P680 site in photosystem II, where the excitons are split into electrons and holes. Although the nanotube concentrator in this work focuses

the light into the near-infrared on spatial concentration, there are applications where the benefits associated with this concentration make up for this energy loss. Many one-dimensional nanostructures have narrow absorption cross-sections, for example, and our antenna concept can be used to systematically increase the absorption bandwidth over a desired window while concentrating the output in space and energy thus potentially leading to new photovoltaics and photodetectors. Future efforts should therefore focus on interfacing such antenna structures with various optoelectronic devices, including photodiodes, photovoltaics and bolometers.

References

1. Currie, M. J., Mapel, J. K., Heidel, T. D., Goffri, S. & Baldo, M. A. High-efficiency organic solar concentrators for photovoltaics. *Science* **321,** 226–228 (2008).
2. Yoon, J. *et al.* Ultrathin silicon solar microcells for semitransparent, mechanically flexible and microconcentrator module designs. *Nature Mater.* **7,** 907–915 (2008).
3. Mühlschlegel, P., Eisler, H-J., Martin, O. J. F., Hecht, B. & Pohl, D. W. Resonant optical antennas. *Science* **308,** 1607–1609 (2005).
4. Taminiau, T. H., Stefani, F. D., Segerink, F. B. & van Hulst, N. F. Optical antennas direct single-molecule emission. *Nature Photon.* **2,** 234–237 (2008).
5. van de Lagemaat, J. *et al.* Organic solar cells with carbon nanotubes replacing In$_2$O$_3$:Sn as the transparent electrode. *Appl. Phys. Lett.* **88,** 233503 (2006).
6. Schuller, J. A., Taubner, T. & Brongersma, M. L. Optical antenna thermal emitters. *Nature Photon.* **3,** 658–661 (2009).
7. Lin, M. F. Optical spectra of single-wall carbon nanotube bundles. *Phys. Rev. B* **62,** 13153–13159 (2000).
8. Yu, Z. & Brus, L. Rayleigh and Raman scattering from individual carbon nanotube bundles. *J. Phys. Chem. B* **105,** 1123–1134 (2001).
9. Wang, F. *et al.* Interactions between individual carbon nanotubes studied by Rayleigh scattering spectroscopy. *Phys. Rev. Lett.* **96,** 167401 (2006).
10. Tan, P. H. *et al.* Photoluminescence spectroscopy of carbon nanotube bundles: Evidence for exciton energy transfer. *Phys. Rev. Lett.* **99,** 137402 (2007).
11. Qian, H. *et al.* Exciton transfer and propagation in carbon nanotubes studied by near-field optical microscopy. *Phys. Status Solidi B* **245,** 2243–2246 (2008).
12. Kato, T. & Hatakeyama, R. Exciton energy transfer-assisted photoluminescence brightening from freestanding single-walled carbon nanotube bundles. *J. Am. Chem. Soc.* **130,** 8101–8107 (2008).
13. Lefebvre, J. & Finnie, P. Photoluminescence and Förster resonance energy transfer in elemental bundles of single-walled carbon nanotubes. *J. Phys. Chem. C* **113,** 7536–7540 (2009).
14. Delaney, P., Choi, H. J., Ihm, J., Louie, S. G. & Cohen, M. L. Broken symmetry and pseudogaps in ropes of carbon nanotubes. *Phys. Rev. B* **60,** 7899–7904 (1999).
15. Kim, W-J., Nair, N., Lee, C. Y. & Strano, M. S. Covalent functionalization of single-walled carbon nanotubes alters their densities allowing electronic and other types of separation. *J. Phys. Chem. C* **112,** 7326–7331 (2008).
16. Arnold, M. S., Green, A. A., Hulvat, J. F., Stupp, S. I. & Hersam, M. C. Sorting carbon nanotubes by electronic structure using density differentiation. *Nature Nanotech.* **1,** 60–65 (2006).
17. Förster, T. 10th Spiers Memorial Lecture. Transfer mechanisms of electronic excitation. *Discuss. Faraday Soc.* **27,** 7–17 (1959).
18. Scardaci, V. *et al.* Carbon nanotubes for ultrafast photonics. *Phys. Status Solidi B* **244,** 4303–4307 (2007).
19. Hertel, T., Fasel, R. & Moos, G. Charge-carrier dynamics in single-wall carbon nanotube bundles: A time-domain study. *Appl. Phys. A* **75,** 449–465 (2002).
20. Lauret, J-S. *et al.* Ultrafast carrier dynamics in single-wall carbon nanotubes. *Phys. Rev. Lett.* **90,** 057404 (2003).
21. Tang, J. *et al.* Assembly of 1D nanostructures into sub-micrometer diameter fibrils with controlled and variable length by dielectrophoresis. *Adv. Mater.* **15,** 1352–1355 (2003).
22. Wang, F., Dukovic, G., Brus, L. E. & Heinz, T. F. Time-resolved fluorescence of carbon nanotubes and its implication for radiative lifetimes. *Phys. Rev. Lett.* **92,** 177401 (2004).
23. Perebeinos, V., Tersoff, J. & Avouris, P. Radiative lifetime of excitons in carbon nanotubes. *Nano Lett.* **5,** 2495–2499 (2005).
24. Qian, H. *et al.* Exciton energy transfer in pairs of single-walled carbon nanotubes. *Nano Lett.* **8,** 1363–1367 (2008).
25. Uchida, T., Tachibana, M. & Kojima, K. Thermal relaxation kinetics of defects in single-wall carbon nanotubes. *J. Appl. Phys.* **101,** 084313 (2007).
26. Hagen, A. *et al.* Exponential decay lifetimes of excitons in individual single-walled carbon nanotubes. *Phys. Rev. Lett.* **95,** 197401 (2005).
27. Trautz, M. Das Gesetz der Reaktionsgeschwindigkeit und der Gleichgewichte in Gasen. Bestätigung der Additivität von C$_v$-3/2R. Neue Bestimmung der Integrationskonstanten und der Moleküldurchmesser. *Z. Anorg. Allg. Chem.* **96,** 1–28 (1916).
28. Manzoni, C. *et al.* Intersubband exciton relaxation dynamics in single-walled carbon nanotubes. *Phys. Rev. Lett.* **94,** 207401 (2005).
29. Vyazovkin, S. Kinetic concepts of thermally stimulated reactions in solids: A view from a historical perspective. *Int. Rev. Phys. Chem.* **19,** 45–60 (2000).
30. Jost, W. The theory of electrolytical charge and diffusion in crystals. II. *Z. Phys. Chem. A* **169,** 129–134 (1934).
31. Zeldowitsch, J. B. On the theory of reactions on powders and porous substances. *Acta Phys.-Chim. URSS* **10,** 583–592 (1939).
32. O'Connell, M. J. *et al.* Band gap fluorescence from individual single-walled carbon nanotubes. *Science* **297,** 593–596 (2002).
33. Buehler, M. J. Mesoscale modeling of mechanics of carbon nanotubes: Self-assembly, self-folding, and fracture. *J. Mater. Res.* **21,** 2855–2869 (2006).
34. Kroeze, J. E., Koehorst, R. B. M. & Savenije, T. J. Singlet and triplet exciton diffusion in a self-organizing porphyrin antenna layer. *Adv. Funct. Mater.* **14,** 992–998 (2004).
35. Gottfried, D. S., Steffen, M. A. & Boxer, S. G. Large protein-induced dipoles for a symmetric carotenoid in a photosynthetic antenna complex. *Science* **251,** 662–665 (1991).
36. Abdula, D. & Shim, M. Performance and photovoltaic response of polymer-doped carbon nanotube p–n diodes. *ACS Nano* **2,** 2154–2159 (2008).
37. Bibby, T. S., Nield, J., Partensky, F. & Barber, J. Oxyphotobacteria: Antenna ring around photosystem I. *Nature* **413,** 590 (2001).
38. Green, B. R. & Parson, W. W. *Light-Harvesting Antennas in Photosynthesis*, Vol. 13 (Kluwer Academic, 2003).

Author contributions

M.S.S. and J-H.H. conceived and designed the experiments. J-H.H. and G.L.C.P. carried out the experiments and theoretical calculation, and J-H.H., G.L.C.P. and M.S.S. analysed the data. D.A.H. designed and built the in-house dual-channel microscope. R.M., D.A.H., W-J.K., P.W.B., C.Y.L., J.H.C., M-H.H., C.S. and C.F. partly assisted in doing experiments and commented on the results. J-H.H., G.L.C.P. and M.S.S. wrote the paper.

Additional information

The authors declare no competing financial interests. Supplementary information accompanies this paper on www.nature.com/naturematerials. Reprints and permissions information is available online at http://npg.nature.com/reprintsandpermissions. Correspondence and requests for materials should be addressed to M.S.S.